Research Article

Eugen Eisfeld* and Johannes Roth

Atomistic simulations of ultra-short pulse laser ablation of aluminum: validity of the Lambert-Beer law

https://doi.org/10.1515/aot-2018-0005
Received January 15, 2018; accepted March 19, 2018; previously published online May 1, 2018

Abstract: Based on hybrid molecular dynamics/two-temperature simulations, we study the validity of the application of Lambert-Beer's law, which is conveniently used in various modeling approaches of ultra-short pulse laser ablation of metals. The method is compared to a more rigorous treatment, which involves solving the Helmholtz wave equation for different pulse durations ranging from 100 fs to 5 ps and a wavelength of 800 nm. Our simulations show a growing agreement with increasing pulse durations, and we provide appropriate optical parameters for all investigated pulse durations.

Keywords: computer modeling; laser ablation; molecular dynamics.

1 Introduction

In the last two decades, ultra-short pulse (USP) laser-metal interactions have been intensively studied due to novel applications, arising from the ability to confine the deposited energy within a small localized volume of the irradiated target material without thermally or mechanically damaging the surrounding regions.

Because of the complex chain of events triggered by laser irradiation including the fast energy absorption by electrons, the electron-phonon energy transfer, transitions to unusual metastable phases, generation of crystal defects, explosive boiling, etc., an experimental identification of the governing phenomena proves to be difficult, thus, limiting the advancement of laser technologies into the realm of nano-scale material processing and fabrication.

Even though recent progress in X-ray and electron diffraction probe methods has provided important insight into fast phase transitions [1, 2], the interpretation of the observations still stands in need of a better understanding of the underlying atomic scale mechanisms leading to this transitions.

In fact, the problem does not lend itself to analytical approaches, and only computer simulations seem capable of dealing with the complex thermo-mechanical pathway leading to ablation. However, computational modeling of these processes is challenging either and requires a combination of different approaches ranging from electronic structure calculations [3], hydrodynamic modeling [4–6], and molecular dynamic (MD) simulations.

In this study we follow the latter approach, since MD simulations have proven to be a promising method, as they provide a means to handle the non-equilibrium phase transformations without the necessity to make a priori assumptions on the mechanisms and kinetics that may take place. A crucial factor in modeling laser ablation is the description of laser energy absorption. A commonly used approach to treat light absorption is the Lambert-Beer (LB) law, which is based on the assumption of a linear relationship between light attenuation and electron number density. In this regard, the reflectivity and the absorption coefficient are supposed to be constants for a given wavelength and material. Our main objective in this study is to investigate the validity of this simplification in the context of USP laser-metal interactions and compare it to a more rigorous method, which involves solving the Helmholtz wave equation for the electromagnetic field.

2 Computational model

In order to take care of the thermal non-equilibrium between electrons and phonons during USP laser-matter

***Corresponding author: Eugen Eisfeld,** Functional Matter and Quantum Technologies, University of Stuttgart, Pfaffenwaldring 57, Stuttgart, Germany, e-mail: eugen.eisfeld@fmq.uni-stuttgart.de
Johannes Roth: Functional Matter and Quantum Technologies, University of Stuttgart, Pfaffenwaldring 57, Stuttgart, Germany

interaction, the simulations are carried out using the well-known two-temperature model (TTM) [7], describing the electrons on a continuum level. Based on the assumption of instant electron thermalization, the model introduces distinct temperatures for the electrons T_e and the ions T_i, the temporal evolution of which is governed by two coupled non-linear differential equations.

The temperature evolution of the free electron subsystem is considered as an advection-diffusion problem, which is solved by means of the finite difference method with a constant cell thickness of approximately 1 nm on a one-dimensional (1D) grid. As shown in Ref. [8], non-local heat transport phenomena may be neglected for rather low peak intensities $I_0 \leq 10^{15}$ W/cm^2 in the case of aluminum. Following Ref. [9], we formulate the energy balance in the Eulerian frame of reference as

$$\frac{\partial(\rho E_e)}{\partial t}+\frac{\partial(\rho E_e v_x^c)}{\partial x}=\frac{\partial}{\partial x}\left(\kappa\frac{\partial T_e}{\partial x}\right)-\gamma(T_e-T_i)+Q_L(t,x), \qquad (1)$$

where ρ, E_e, and v_x^c correspond to the ionic density, the free electrons' specific energy, and the center-of-mass velocity along the x-direction, respectively. The laser source term $Q_L(t, x)$ is described in Section 2.1. The electronic heat conductivity $k(T_e, \rho)$ and the electron-ion coupling factor $\gamma(T_e, \rho)$ controlling the heat exchange between the subsystems are calculated by wide-range models, interpolating between the metallic and plasma state as described in Ref. [10].

The ionic heat conductivity is automatically accounted for by the particles' equations of motion with an additional friction term, while the MD/TTM coupling is established by a Langevin thermostat. More details regarding the TTM/MD coupling can be found in Refs. [11–15] and references therein. For the inter-atomic interactions, we use the EAM potential developed in Ref. [16], which was designed to reproduce the cold stress curves, the shock Hugoniot, and the melting point with good accuracy.

In order to improve performance, we apply Strang's operator-splitting scheme [17] and split the advection-diffusion problem Eq. (1) into two separate problems, which is second-order accurate in time and introduces an error of only $\propto\tau^3$ [18], where τ represents the time step. Assuming that bound and free electrons move together with their corresponding atoms, the advection step is given as [9]

$$\begin{aligned}N_j(t+\tau)E_{e,j}(t+\tau)&=N_j(t)E_{e,j}(t)+N^+_{j-\frac{1}{2}}(t)E_{e,j-1}(t)\\&-N^-_{j-\frac{1}{2}}(t)E_{e,j}(t)-N^-_{j+\frac{1}{2}}(t)E_{e.j}(t)+N^+_{j+\frac{1}{2}}(t)E_{e,j+1}(t),\end{aligned} \qquad (2)$$

where N_j is the number of atoms in the jth cell at time t, $N^-_{j-1/2}$ and $N^-_{j+1/2}$ correspond to the number of atoms flowing out of cell j into cell $j-1$ across the boundary $j-1/2$ and the number of atoms flowing out of cell j into cell $j+1$ across the boundary $j+1/2$, respectively. Similarly, $N^+_{j-1/2}$ and $N^+_{j+1/2}$ represent the atomic flux into cell j from cell $j-1$ and $j+1$ across the boundaries $j-1/2$ and $j+1/2$.

For the relation between E_e and T_e we use McCloskey's electronic equation of state, which provides a suitable description of the thermodynamic behavior of metals for a very wide range of temperature and compression [19].

2.1 Laser energy absorption

In this study, we compare two different methods to describe the absorbed laser power-density $Q_L(x, t)$. In both cases, the reflection of light needs to be accounted for. We assume that the laser energy is predominately absorbed by free electrons via inverse Bremsstrahlung. Further, we neglect any non-linear effects, which is justified as we are concerned with rather low intensities. For a Gaussian pulse, the LB law gives the absorbed power density

$$Q_L(x,t)=(1-R)\mu\exp(-\mu x)\frac{F_0}{\tau_{\mathrm{FWHM}}}\sqrt{\frac{\log(2)}{\pi}}\,8\exp\left(-\left(\frac{t-t_0}{\tau_{\mathrm{FWHM}}}\right)^2\right), \qquad (3)$$

where R is the surface-reflectivity, μ is the absorption coefficient, x is the position within the material along the laser irradiation direction relative to the surface, t_0 is the time of peak intensity, τ_{FWHM} is the pulse duration of full width at half maximum, and F_0 is the laser fluence, which is related to the peak intensity via $F_0 = I_o\tau_{\mathrm{FWHM}}\sqrt{\pi/\log(16)}$.

For the second method, which implicitly includes the dynamic reflection at the surface as well as within the material itself, the interaction between the linear polarized laser, incident along the x-direction and the metal is described by the Helmholtz wave equation. Here, we assume 1D geometry, and using the slowly varying envelope approximation, the magnitude of the electric field envelope $E(x, t) = E_y(x, t)$ is obtained from solving

$$\frac{\partial^2 E(x,t)}{\partial x^2}+\left(\frac{\omega_0}{c}\right)^2\epsilon(x,T_e,T_i,\rho,\omega_0)E(x,t)=0, \qquad (4)$$

with appropriate boundary conditions according to the continuity of tangential field components [20]. Here, ω_0 is the laser angular frequency, and c is the vacuum speed of light. The complex permittivity $\epsilon(x, T_e, T_i, \rho, \omega_0)$ of the

material is obtained from a wide-range model proposed in Refs. [10] and [20–22]. In a nutshell, the model interpolates between the Drude-like phenomenological model with an additional inter-band transition term for the cold metallic state and a plasma model for the hot state above the Fermi temperature.

Equation (4) is solved assuming the permittivity to be approximately constant within each individual cell by means of the analytical transfer-matrix method (TMM) [20, 23]. Then, for the *j*th cell, the absorbed power density is related to the divergence of the Poynting vector and is calculated from [9]

$$Q_{L,j} = \frac{I(t)\omega_0 / c\ \mathrm{Im}(\epsilon_j)}{x_{j+1} - x_j} \int_{x_j}^{x_{j+1}} |E_j|^2 \mathrm{d}x. \tag{5}$$

We solve Eq. (5) using a fourth-order Runge-Kutta algorithm with an adaptive step size.

2.2 Pressure-absorbing boundary conditions

In order to reduce the reflection of pressure and rarefaction waves at the rear side of the sample, we enforce pressure-absorbing boundary conditions for the very last layer of atoms. In this regard, we follow Ref. [24] and consider a monochromatic wave solution for the atomic motion. Instead of integrating the particles' equations of motion resulting from the inter-atomic potential, these atoms are displaced according to

$$\begin{aligned}\dot{\boldsymbol{u}}_{0.n,m} = &\sqrt{\frac{k}{m}}\boldsymbol{u}_{0,n,m}\begin{pmatrix} -4 & 0 & 0 \\ 0 & -2\sqrt{2} & 0 \\ 0 & 0 & -2\sqrt{2} \end{pmatrix} \\ &+\sqrt{\frac{k}{m}}\boldsymbol{u}_{0,n,m}\begin{pmatrix} 1 & 0 & 0 \\ 0 & \frac{\sqrt{2}}{2} & 0 \\ 0 & 0 & \frac{\sqrt{2}}{2} \end{pmatrix}\cdot(\boldsymbol{u}_{1,n,m+1} + \boldsymbol{u}_{1,n,m-1} + \boldsymbol{u}_{1,n+1,m} \\ &+\boldsymbol{u}_{1.n-1,m)} - \frac{1}{4}(\dot{\boldsymbol{u}}_{1,n,m+1} + \dot{\boldsymbol{u}}_{1,n,m-1} + \dot{\boldsymbol{u}}_{1,n+1,m} + \dot{\boldsymbol{u}}_{1,n-1,m}).\end{aligned} \tag{6}$$

Here, $\boldsymbol{u}_{i,n,m}$ is the displacement vector of an atom at the lattice site *l*, *n*, *m*. For $l=0$, we refer to an atom of the boundary layer (last layer), while for $l=1$, the displacement vectors refer to the nearest neighbors of the corresponding boundary atom (second to last layer, see Figure 1). Further, *m* is the atom's mass, and *k* is a force constant for which we use $k = 13.28\ \mathrm{kg/s^2}$.

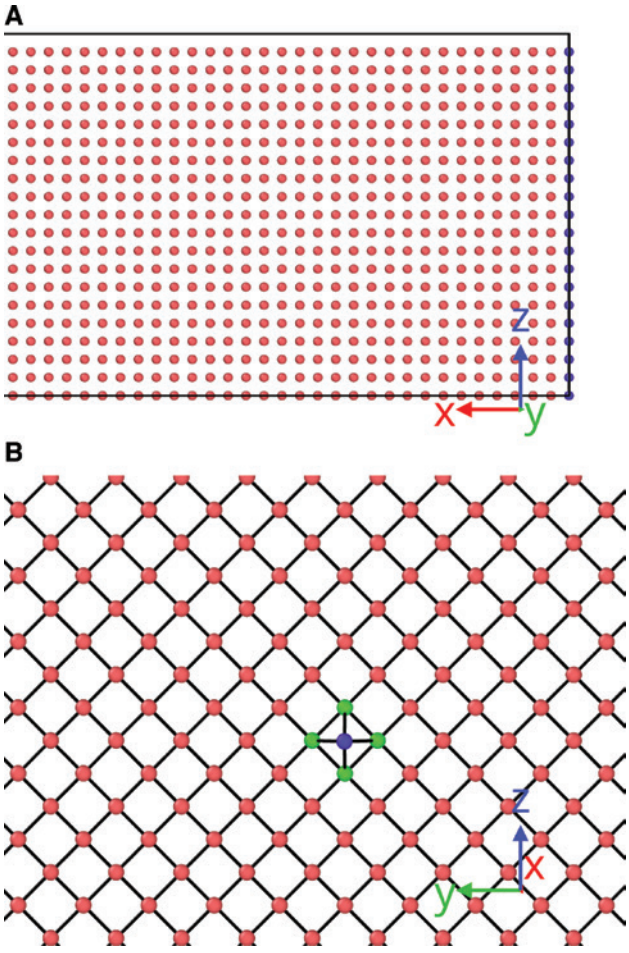

Figure 1: Illustration of boundary layer of fcc-(100) aluminum sample (A) (blue atoms) and schematic representation of nearest neighbors (green) for a single boundary layer atom (B).

2.3 Computational setup

For all simulations, our target is a single crystal aluminum sample of size 0.8 μm × 10 nm × 10 nm of crystallographic orientation (1, 0, 0) along the *x*-direction and periodic boundary conditions applied along the *y*- and *z*-directions. The laser, having a wavelength of 800 nm and a fluence of 2 J/cm² irradiates along the *x*-direction at normal incidence. In total, six different situations with varying pulse durations are compared. It has to be noted that the thermo-mechanical behavior of the sample strongly depends on the cross-section. However, in Ref. [16], it was shown that for two different samples, the larger one having a cross section of 49 nm × 49 nm and the smaller one 7 nm × 7 nm, the differences regarding the threshold temperatures for ablation and spallation are only about 2%. Still, we have to emphasize that this behavior must not be extrapolated to larger fluences, in general, and requires careful investigation of the cross-section dependence. As this study

is mainly concerned with differences resulting from different theoretical approaches rather than experimental validation, we assume a negligible influence of the cross-section for the chosen fluence.

3 Results and discussion

For the first set of simulations, the laser energy deposition is computed by means of the transfer-matrix method. The results are then used to calculate averaged optical parameters, which are needed for the corresponding simulations using the Lambert-Beer law. In order to make the comparison as fair as possible, for each situation, an individual absorption coefficient is calculated. This is done by time averaging the permittivity of the surface according to

$$\bar{\epsilon} = \tau_{\text{pulse}}^{-1} \int \epsilon_{\text{surface}}(t)\,\mathrm{d}t, \tag{7}$$

where $\tau_{\text{pulse}} \approx 3\tau_{\text{FWHM}}$ corresponds to the duration of laser-metal interaction. It should be noted that this averaging is not performed across the true skin depth. Instead, only the first non-empty cell within the finite-difference grid is used, which has a thickness of about 1 nm. Then, the absorption coefficient is obtained from

$$\mu = \frac{2k\omega_0}{c}, \tag{8}$$

with the extinction coefficient

$$k = \sqrt{\frac{1}{2}\left(\sqrt{\mathrm{Re}(\bar{\epsilon})^2 + \mathrm{Im}(\bar{\epsilon})^2} - \mathrm{Re}(\bar{\epsilon})\right)}, \tag{9}$$

Likewise, for the reflectivity, an averaged value is used, which is easily obtained from the ratio of the total absorbed fluence and the incident fluence according to $R = 1 - F_{\text{abs}}/F_0$ (see Figure 2). The parameters for the LB simulations are summarized in Table 1. In line with the suggestion of one of the reviewers, we tested an additional scheme to determine μ: For this purpose, the absorbed power density profile at $t = t_0$ was inspected, and the data was fitted with the natural logarithm of Eq. (3), which has the form $\log(Q(x)) = a - \mu x$, with a being a constant. Hence, the slope gives an estimate of the absorption coefficient across the full laser-affected depth. In addition, a combination of both schemes was tested by applying the procedure of the second method to every time step during the laser-metal interaction, followed by time averaging the summation of all $\mu(t)$ similar to Eq. (7). In the following, we will refer to results obtained from these different schemes as LB(1), LB(2), and LB(3), respectively.

First, the resulting ablation depths are compared. This is done by summing the mass densities of the ablated cells and relating them to the original solid density $\rho_0 \approx 2.7\ \mathrm{g/cm^3}$ according to

$$d_{\text{abl}} = \sum_i \text{cellwidth} \cdot \rho(i)/\rho_0, \tag{10}$$

where i runs over all ablated cells. It should be noted that the ablation depth can be determined more accurately by counting the ablated atoms. However, the procedure according to Eq. (11) can be more easily automated, and more importantly, it does not require to save large files containing every atom's coordinates. For Figure 6, the former method was used, while the final ablation depths, depicted in Figure 3, were determined by the latter one. The resulting ablation depths as a function of the pulse duration are given in Figure 3A, while Figure 3B illustrates the relative differences between the TMM and LB simulations.

Overall, it seems like the LB approach becomes more and more accurate for growing pulse durations, except for LB(3), which works better for short durations $\tau_{\text{FWHM}} \leq 1$ ps. For longer pulses, however, the LB(3) scheme is not appropriate as the $\mu(t)$ averaging is carried out over the full laser-metal interaction timespan, placing too much emphasis on those $\mu(t)$ where the intensity is rather low, resulting in unfavorable lowering of the mean value $\mu_2(t)$. A more suitable approach would be a weighted averaging with respect to the laser intensity, thus, emphasizing the more important time-frame of laser-metal interaction. This is evident from the growing agreement of the LB(2) approach, where only the absorption coefficient at the time of peak intensity is used. For $\tau_{\text{FWHM}} = 5$ ps, the difference amounts to only about 4.5% with respect to the result from the TMM simulation. For short pulses, the system reacts very sensitively to changes in reflectivity and the absorption coefficient, as this drastically affects the temperature profiles within the target, as depicted in Figure 4A. For all pulse durations, the Helmholtz approach yields steeper profiles for the deposited energy compared to the LB law. However, with decreasing pulse duration, this difference becomes more pronounced. In contrast, for longer pulses, there is enough time for diffusion to relativize this difference.

In the remaining discussion, we focus on the comparison between the LB(1) scheme and the TMM case, as this scheme shows the least fluctuations in ablation depth as a function of pulse duration.

Interestingly, for $\tau_{\text{FWHM}} = 100$ fs, the resulting ablation depths turn out to be very close even though the difference in electron-temperature profiles is comparable to $\tau_{\text{FWHM}} = 200$ fs. In order to further examine this coincidence,

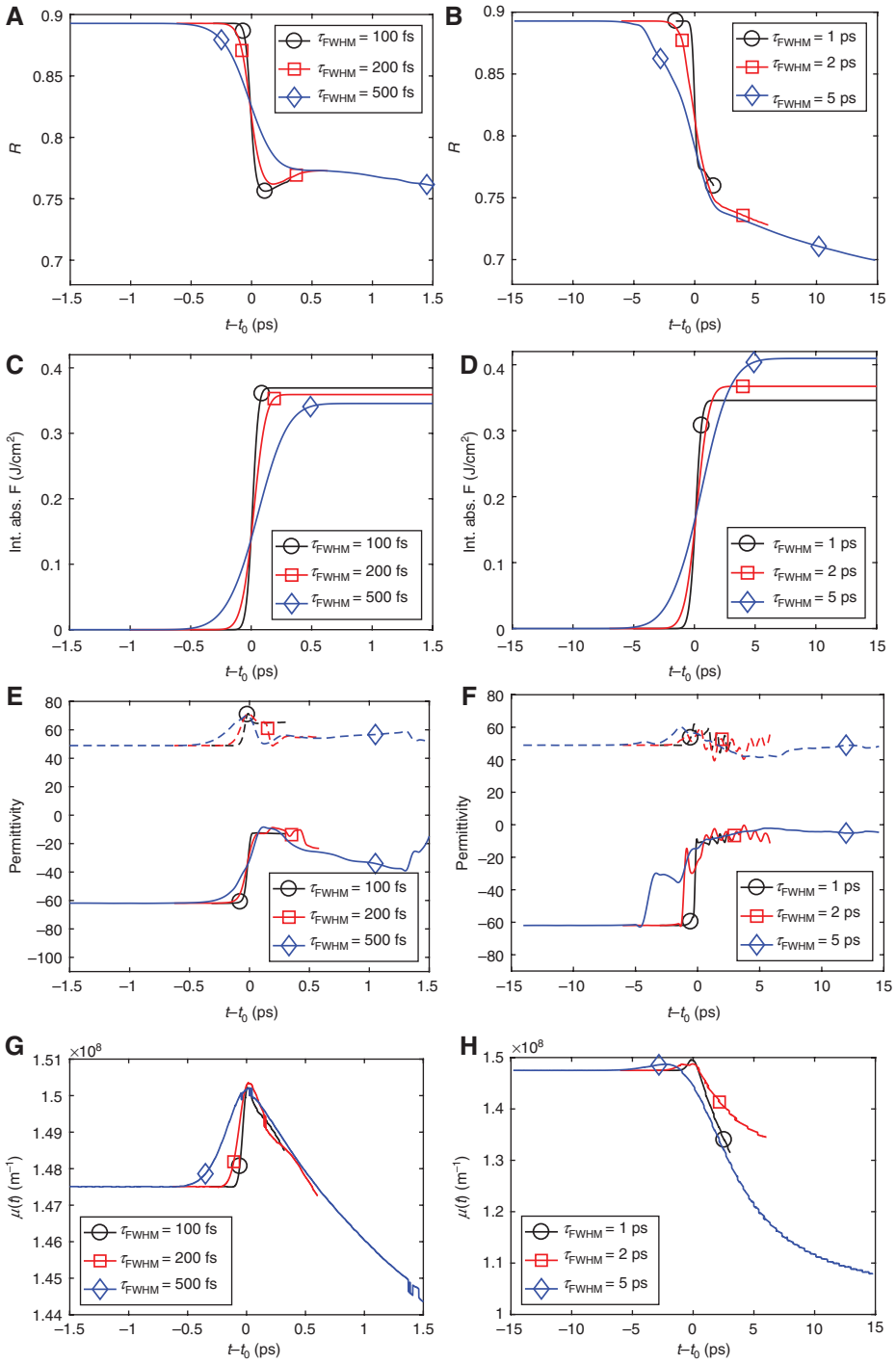

Figure 2: Transient reflectivities as well as resulting integrated absorbed fluence during laser-matter interaction obtained from simulations using the transfer matrix method for sub-ps pulses (A, C) and ps (B, D). In addition, we present the imaginary (dashed) and real (continous) parts of permittivity (E, F) for the first non-empty cell as well as the absorption coefficients according to scheme LB(3) in subfigures (G, H).

it is worth to inspect the temporal evolution of the total electronic specific energy in Figure 4B for the time span just before ablation starts. The cumulative integrated difference in electronic specific energy between the TMM and LB simulations can be interpreted as a measure of how similar the electron-phonon equilibration dynamics are. In this regard, it is evident that for $\tau_{\mathrm{FWHM}} = 100$ fs, this quantity turns out to grow slower compared to the other

Table 1: Averaged parameters used to compute laser-energy absorption by means of the Lambert-Beer law.

τ_{FWHM} ps	F_{abs} Jcm^{-2}	$\bar{R}$	Re($\bar{\epsilon}$)	Im($\bar{\epsilon}$)	k	μ_1 10^8m^{-1}	μ_2 10^8m^{-1}	μ_3 10^8m^{-1}
0.1	0.37	0.82	−56.21	44.08	3.69	0.58	1.49	1.15
0.2	0.36	0.82	−41.30	37.31	3.03	0.48	1.47	1.14
0.5	0.35	0.83	−43.23	45.33	2.94	0.46	1.47	1.27
1	0.35	0.83	−41.43	41.99	2.91	0.46	1.49	1.29
2	0.37	0.82	−32.72	42.97	2.35	0.37	1.48	1.29
5	0.41	0.80	−29.87	43.89	2.15	0.34	1.45	1.31

The absorption coefficients have been determined according to three different approaches as stated in the text.

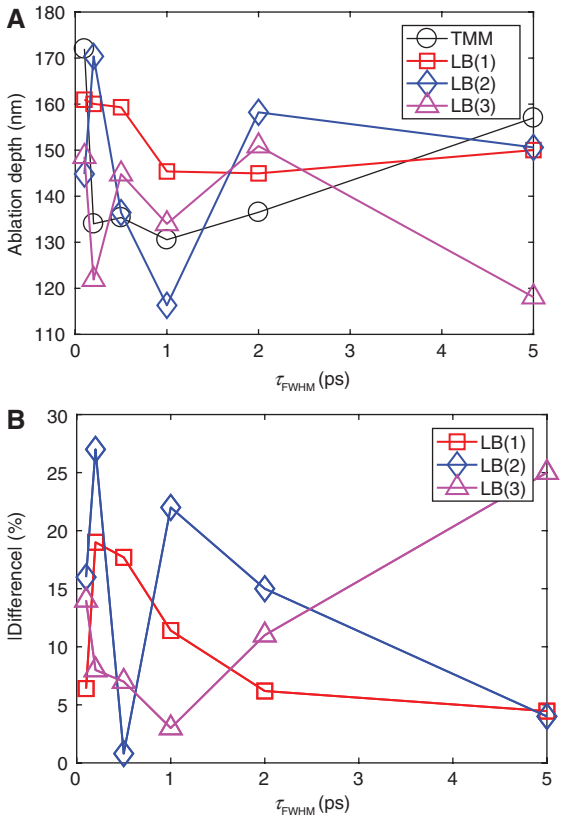

Figure 3: Comparison of simulated ablation depths with respect to the employed energy deposition method (A) and the relative difference of the results (B).

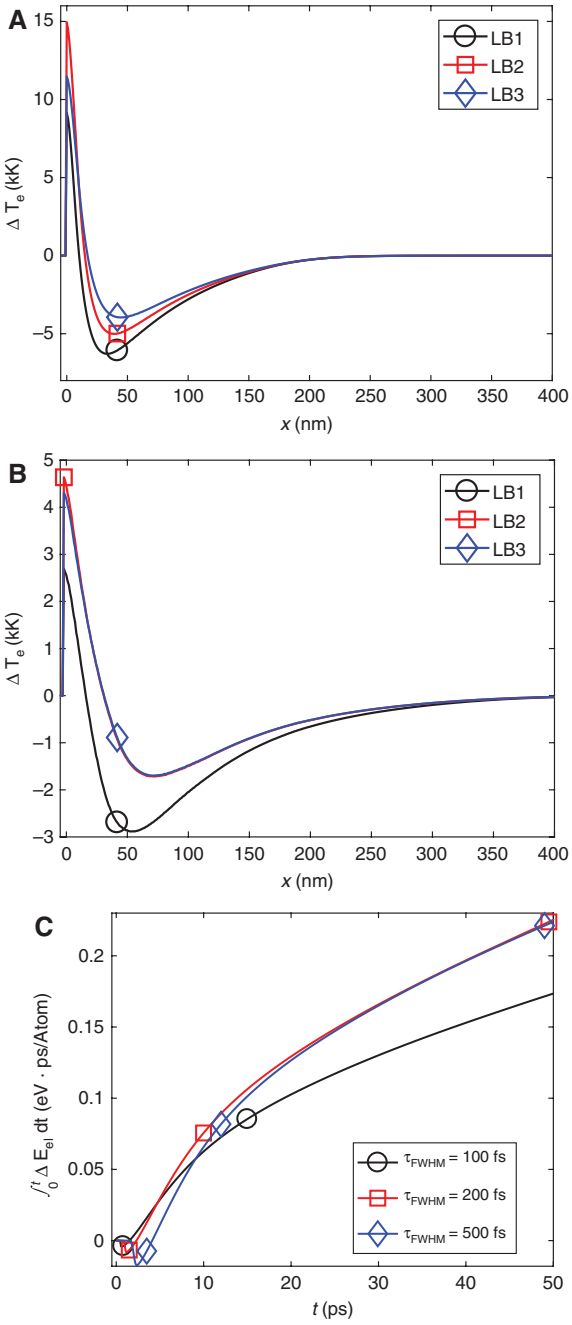

Figure 4: Difference in spatial electron-temperature profiles $\Delta T_e = T_e^{TMM} - T_e^{LB}$ at $t = t_0$ for a pulse duration of 200 fs (A) and 5 ps (B) and temporal evolution of cumulative integrated differences in specific electronic energy for the LB(1) case (C).

sub-ps pulses. This is supposed to be a lucky coincidence, resulting from the complex interplay of temperature-dependent thermal conductivity, electron-ion coupling and permittivity.

As a consequence, the ablation behavior for both methods is very similar in this case. This can be seen in Figure 5 illustrating the correlation between the evolution of ablation depth and the surface area of subsurface pores. The area is calculated from a surface construction algorithm given in Ref. [25], where the volume below the surface is analyzed using a virtual probe sphere with a radius of 0.5 nm.

The ablation depth is calculated from Eq. (11), where cells are regarded as ablated if they are separated from the surface by more than 5 nm of empty space. As is evident

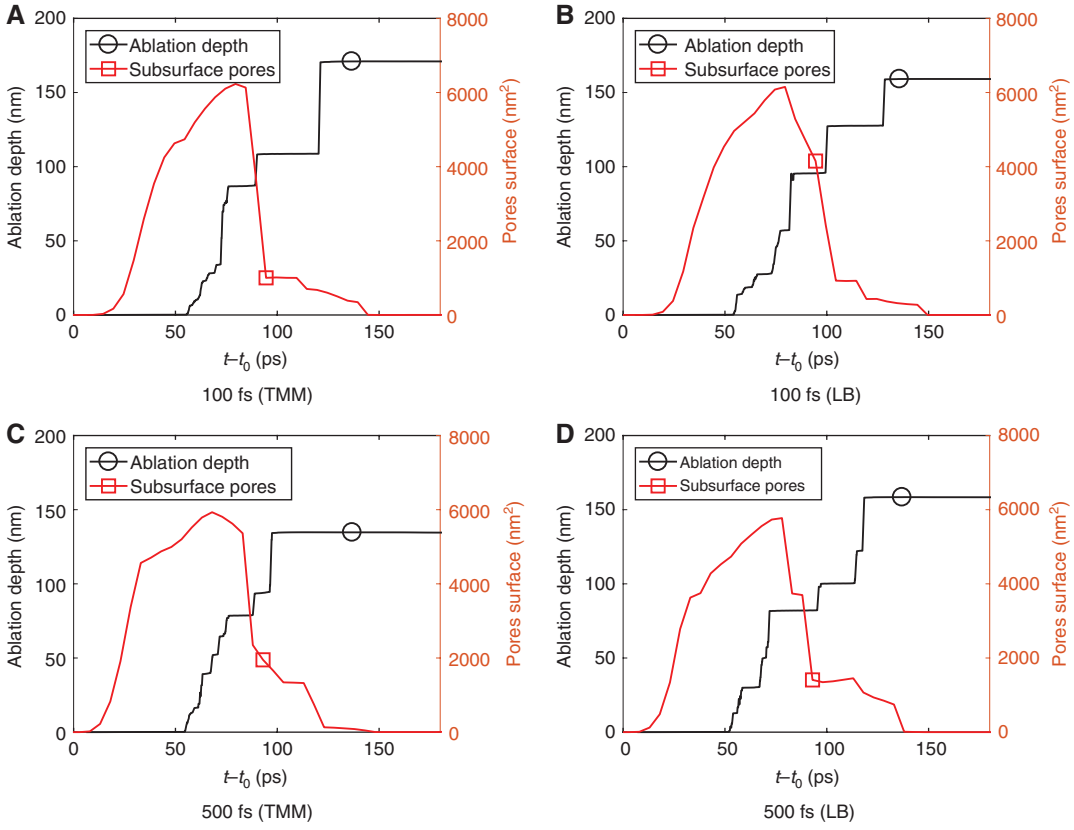

Figure 5: Temporal evolution of ablation depth and surface area of pores below the surface $\tau_{FWHM} = 100$ fs (A, B) and $\tau_{FWHM} = 500$ fs (C, D) using the TMM compared to the LB(1) case.

from all the figures, pores appear around 10 ps after the pulse, while ablation starts around 50 ps. The ablation depth continuously grows with the surface area of the pores until about 100 ps. For all simulations, the governing ablation mechanism resembles a combination of spallation and explosive boiling: pores nucleate, grow, and coalesce even before a tensile wave is generated as can be seen in Figure 6.

However, the passage of the rarefaction wave further increases the surface area of the pores, eventually resulting in separation and ejection of melted layers from the front of the target [11, 26].

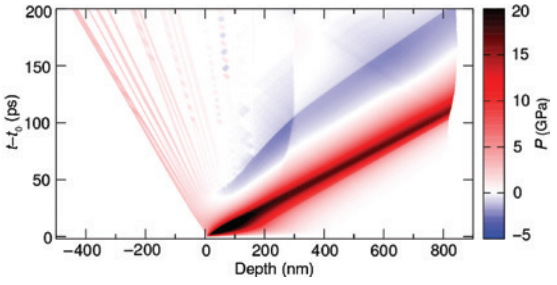

Figure 6: Hydrostatic pressure contour plot for $\tau_{FWHM} = 500$ fs.

After about 100 ps, the correlation between further ablation and the number of subsurface pores seems to be less significant. This late ablation events result from deeper regions within the target, where the temperature is lower, and explosive boiling is unlikely to occur. However, the tensile stresses of the rarefaction wave are increasing with depth, thus, enabling further ablation. This is not the case for the TMM simulation of $\tau_{FWHM} = 500$ fs. As opposed to the LB case, the initial increase in the surface area of pores is more rapid due to the higher surface temperature suggesting an enhanced involvement of explosive boiling. Consequently, the resulting pressure and tensile waves are slightly more intense. Nonetheless, this is not sufficient for further spallation. On the other hand, using the LB law gives rise to higher temperatures at larger depths, thus, reducing the lattice's resistance toward the arriving tensile wave in deeper regions. Likewise, for pulse durations of 1 ps and 2 ps, this 'lattice-softening' in deeper regions is the reason for larger ablation depths when using the LB law. For $\tau_{FWHM} = 5$ ps, the situation regarding ablation depths is vice versa. However, for this specific case, this minor discrepancy may be neglected. All in all, the simulations

show that approximating laser light absorption of aluminum by the Lambert-Beer law is sufficiently accurate for pulse durations above ≈2 ps, even for absorbed fluences of more than 0.35 J/cm^2, which exceed the threshold fluences for ablation ≈60 mJ/cm^2 and spallation ≈120 mJ/cm^2 by far [16].

4 Conclusion

In summary, we performed hybrid MD/TTM simulations of single-pulse laser ablation of single crystalline aluminum targets for different pulse durations. Laser light absorption was modeled using either the transfer matrix method, where the Helmholtz wave equation for the electromagnetic field is solved or the Lambert Beer law, where the absorption coefficient is obtained from three different approaches. For sub-ps pulses, the simulations reveal a maximum discrepancy between these methods of about 25% in the resulting ablation depths, indicating the importance of the dynamical reflectivity and absorption depth, which cannot be approximated by time-averaged optical properties. With increasing pulse durations, the differences become smaller, and already for a 5 ps pulse, the disparity drops below 5% for two of the LB-approaches. This is attributed to slower heating and the elevated thermal diffusion of the excited electrons, resulting in only minor differences in the spatial lattice temperature profiles.

Funding: Deutsche Forschungsgemeinschaft, Funder Id: 10.13039/501100001659, Grant Number: SFB 716, subproject B5.

References

[1] B. Lin and H. E. Elsayed-Ali, Surf. Sci. 498, 275–284 (2002).
[2] K. Sokolowski-Tinten, C. Blome, J. Blums, A. Cavalleri, C. Dietrich, et al., Nature 422, 287–289 (2003).
[3] Z. Lin, L.V. Zhigilei and V. Celli, Appl. Phys. A 77, 776 (2008).
[4] J. P. Colombier, P. Combis, E. Audouard and R. Stoian, New J. Phys. 14, 13039 (2012).
[5] J. P. Colombier, P. Combis, A. Rosenfeld, I. V. Hertel, E. Audouard, et al., Appl. Surf. Sci. 74, 311 (2006).
[6] N. M. Bulgakova, R. Stoian, A. Rosenfeld, I. V. Hertel and E. E. B. Campbell, Phys. Rev. B 69, 97 (2004).
[7] M. Kaganov, I. Lifshitz and L. Tanatarov, J. Exp. Theor. Phys. 4, 173–178 (1957).
[8] N. E. Andreev, V. V. Kostin and M. E. Veisman, Phys. Scr. 58, 486 (1998).
[9] M. E. Povarnitsyn, V. B. Fokin, P. R. Levashov and T. E. Itina, Phys. Rev. B 92, 232 (2015).
[10] M. E. Povarnitsyn and N. E. Andreev, J. Phys.: Conf. Ser. 774, 12105 (2016).
[11] L. V. Zhigilei, D. S. Ivanov, E. Leveugle, B. Sadigh and E. M. Bringa, in: 'Computer Modeling of Laser Melting and Spallation of Metal Targets', (SPIE, Taos, NM, 2004) p. 505.
[12] S. Scharring, D. J. Förster, H.-A. Eckel, J. Roth and M. Povarnitsyn, in: HPLA/BEP 2014.
[13] W. E. Nagel, D. B. Kröner, M. M. Resch, J. Roth, C. Trichet, et al., Eds., in: 'Laser Ablation of Metals: High Performance Computing in Science and Engineering 10', (Springer, Berlin Heidelberg, 2011).
[14] J. Roth, A. Krauß, J. Lotze and H.-R. Trebin, Appl. Phys. A 117, 2207–2216 (2014).
[15] D. S. Ivanov and L. V. Zhigilei, Phys. Rev. B 68, 433 (2003).
[16] V. V. Zhakhovskii, N. A. Inogamov, Y. V. Petrov, S. I. Ashitkov and K. Nishihara, Appl. Surf. Sci. 255, 9592–9596 (2009).
[17] G. Strang, SIAM J. Numer. Anal. 5, 506–517 (1968).
[18] H. Holden, K. Karlsen, K.-A. Lie and N. H. Risebro, in 'Splitting Methods for Partial Differential Equations with Rough Solutions', (European Mathematical Society Publishing House, Zuerich, Switzerland, 2010).
[19] D. J. McCloskey, An Analytic Formulation of Equations of State, available at https://www.rand.org/pubs/research_memoranda/RM3905.html.
[20] M. E. Povarnitsyn, N. E. Andreev, P. R. Levashov, K. V. Khishchenko and O. N. Rosmej, Phys. Plasmas 19, 23110 (2012).
[21] N. E. Andreev, M. E. Veisman, V. P. Efremov and V. E. Fortov, High Temp. 41, 594–608 (2003).
[22] M. B. Agranat, N. E. Andreev, S. I. Ashitkov, M. E. Veĭsman, P. R. Levashov, JETP Lett. 85, 271–276 (2007).
[23] M. Born and E. Wolf, in 'Principles of Optics: Electromagnetic Theory of Propagation, Interference and Diffraction of Light', 7th ed., (Cambridge University Press, Cambridge, New York, 1999).
[24] M. Fang, S. Tang, Z. Li and X. Wang, Comput. Mech. 50, 645–655 (2012).
[25] A. Stukowski, J. Met. 66, 399–407 (2014).
[26] C. Wu and L. V. Zhigilei, Appl. Phys. A 114 11–32 (2014).